Systematic two-scale image analysis of extreme deformations in soft architectured sheets

Filippo Agnelli, Pierre Margerit, Paolo Celli, Chiara Daraio, Andrei Constantinescu

Systematic two-scale image analysis of extreme deformations in soft architectured sheets

Filippo Agnelli[a], Pierre Margerit[a], Paolo Celli[b,c], Chiara Daraio[c], Andrei Constantinescu[a,*]

[a]*Laboratoire de Mcanique des Solides, CNRS, cole polytechnique, Institut polytechnique de Paris, 91128 Palaiseau, France*
[b]*Department of Civil Engineering, Stony Brook University, Stony Brook, NY 11794, USA*
[c]*Division of Engineering and Applied Science, California Institute of Technology, Pasadena, CA 91125, USA*

Abstract

The multi-scale nature of architectured materials raises the need for advanced experimental methods suitable for the identification of their effective properties, especially when their size is finite and they undergo extreme deformations. The present work demonstrates that state-of-the art image processing methods combined with numerical and analytical models provide a comprehensive quantitative description of these solids and their global behaviour, including the influence of the boundary conditions, of the manufacturing process, and of geometric and constitutive non-linearities. To this end, an adapted multi-scale digital image correlation analysis is used to track both elongations and rotations of particular features of the unit cell at the local and global (homogenized) scale of the material. This permits to observe with unprecedented clarity the strain fields for various unit cells in the structure and to detect global deformation patterns and heterogeneities of the homogenized strain distribution. This method is here demonstrated on elastic sheets undergoing extreme longitudinal and shear deformations. These experimental results are compared to non-linear finite element simulations, which are also used to evaluate the effects of manufacturing imperfections on the response. A skeletal representation of the architectured solid is then extracted from the experiments and used to create a purely-kinematic truss-hinge model that can accurately capture its behaviour. The analysis proposed in this work can be extended to guide the design of two-dimensional architectured solids featuring other regular, quasi-regular or graded patterns, and subjected to other types of loads.

Keywords: auxetic, architectured solids, soft materials, digital image correlation, skeletal representation

1. Introduction

Architectured sheets are a particular class of two-dimensional solids whose patterned designs are tailored to achieve a variety of exceptional mechanical behaviours, including extreme stretchability, auxeticity and morphing capabilities [1–8]. They are increasingly seen as applicable to fields ranging from stretchable electronics, medical and biomedical engineering [9–13], to the sport equipment and textile industries [14–18], and they have witnessed significant advances in their design and fabrication. When it comes to designing techniques, modern numerical methods such as shape and topology optimization [19, 20] have become prevalent in this realm, leading to more sophisticated and often unimaginable geometries [21–25]. Present day techniques even permit to incorporate geometric non-linearity and manufacturability constraints in the design optimization [26–28]. At the same time, digitally controlled manufacturing techniques such as photo-lithography [29], 3-d printing [30, 31], water jetting [32] and laser cutting [2, 33] now permit to fabricate architectured solids with unprecedented complexity and at a continuously decreasing cost.

Despite these breakthroughs, unleashing the potential of these systems demands advanced methods suitable for the experimental investigations on the deformation patterns and mechanical behaviour, which are to date in their early stages. In practice, specimens designed for mechanical characterization usually exhibit highly heterogeneous strain fields associated with: (i) their intrinsic multi-scale behaviour, that can be separated between the microscopic scale (material continuum) and the macroscopic scale (the global scale of the specimen); (ii) boundary layers that emerge from the boundary conditions and the finite size of the specimens; (iii) inherent anisotropic effective properties; (iv) sensitivity to shape imperfections. This high heterogeneity of the strain fields limits the level of identification that can be achieved from experimental measurements. For example, qualitative experimental insights on the behaviour of regions where macroscopic strains can be considered homogeneous have been reported in [33, 34]. As a consequence, only the central region of a specimen is typically used to validate numerical predictions [27, 35, 36], especially when one wants to compute the homogenised properties of the medium. It should be noted that the interaction of scales is a key point for quantitatively understanding the behaviour of architectured solids. Experimentally, a precise separation between micro-scale and macro-scale kinematic fields based on a first-order expansion of the fields can be performed, as illustrated in [37]. However, to the best of our knowledge, this technique has hardly ever been adopted in the context of architectured solids, being limited to the case of perforated sheets [34]. The complexity of this interaction of scales has additionally motivated the de-

*Corresponding author
Email address: andrei.constantinescu@polytechnique.edu (Andrei Constantinescu)

velopment of reduced-order models [38–41], to provide a better understanding of the underlying mechanisms and guidelines for design strategies. These reduced models often represent an idealised version of the unit-cell, and are inaccurate if not accompanied by robust experimental methods for the calibration of their parameters. On the opposite side of the spectrum of available numerical tools, lie models based on the complete description of the specimen, which are typically used to provide a direct term of comparison with experimental results [42–44]. The (often small) discrepancies between simulated and measured response have origins at multiple scales. They are either found at the microscopic scale, where the manufacturing process is a source of shape imperfections, or at the macroscopic scale, where applied boundary conditions may distort the unit cell pattern.

The present work aims to demonstrate that various state-of-the art methods in image processing can be combined to provide comprehensive data on the multi-scale response of architectured sheets. Our procedure, applicable to any two-dimensional architectured solids, is here applied to investigate the deformation mechanisms of a soft auxetic sheet under extreme longitudinal and shear loading. The acquired images of the structure are first used to identify its exact geometry, which may differ from the designed one due imperfections in the fabrication process. Meshes are built directly from the identified shape and used both for the measurement of the full kinematic field (via Digital Image Correlation) as for the numerical computations (via the Finite Element Method). It is shown that doing so significantly improves the match between measurements and numerical predictions with respect to models that rely on the as-designed specimen geometry. This highlights the high sensitivity of the mechanical response of the specimen to geometrical imperfections. Then, we provide a two-scale analysis of the measured kinematic field: (i) at the continuum material level (microscopic scale) and (ii) at the unit cell level (macroscopic scale). This leads to the quantification of the macroscopic strain heterogeneities and the characteristic deformation patterns, which are influenced by the boundary conditions as well as the inherent Poisson's ratio of the micro-structure. The kinematic analysis is complemented by a procedure aiming at extracting the skeletal representation of the specimen from the experimentally-recorded images. This experimentally-extracted skeleton, whose shape changes during the deformation process, is then used to identify the parameters for an accurate reduced-order model of the architectured solid.

The study is organized as follows: Section 2 provides details on fabrication, experimental setups, testing methods, material models and modelling strategy. The results are reported in Section 3, and include the material constitutive law calibration, the multi-scale experimental analysis and the numerical simulations. The skeletal representation of the architectured sheet geometry is discussed in the same Section. A short summary in Section 4 concludes the paper.

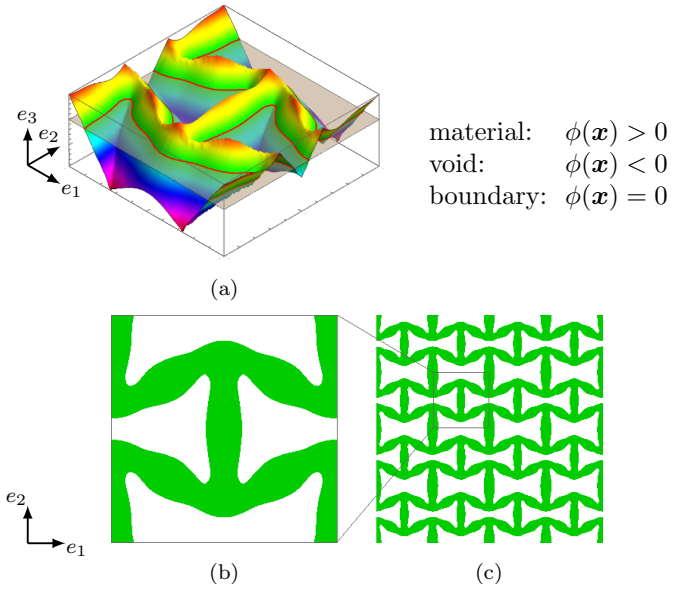

Figure 1: Geometry of the re-entrant honeycomb. (a) 3-d representation of the level set function (signed distance function) ϕ, sliced by the plane $z = 0$. The function results from the topology optimization procedure of [36]. (b) Unit cell, the boundary is described with the zero level set. The material volume fraction is $f = 0.48$. (c) 4×4 repetitive array of unit cells.

2. Materials and methods

2.1. Unit cell architecture

To demonstrate our approach, we choose to analyse the periodic auxetic micro-structure recently proposed in [36]. The design results from a topology optimization procedure combining the level set method and the asymptotic homogenization theory [25, 45] aiming to maximize the auxetic behaviour. The level set function ϕ serves as a base to define the material distribution in the unit cell (see Figure 1(a)), and is defined as the *signed distance function*, for smoothness and regularity purposes. The optimization problem is formulated as a constrained minimization problem, where the objective functional to be minimized is a squared distance between the effective elastic moduli over the unit cell and a prescribed elastic moduli $\mathbb{C}^T$ (the superscript T stands for target, refer to [36] for further details). This type of objective functional was first proposed in [46]. Starting from the architecture provided in [36], we merely operate a vertical shift to obtain a symmetric design. The resulting unit cell is depicted in Figure 1(b,c). The designed geometry is a re-entrant honeycomb with a couple of peculiar features. First, the structure is characterised by a repetitive alternation of two types of concave hexagons. Second, the trusses do not have constant width, *i.e.* the linkages appear slightly thinner than the cores of the bars. This feature is shared with other shapes available in the literature, that also stem from topology optimization algorithms based on the level set method aiming to minimize the Poisson's ratio [21, 22]. It is also similar to the bi-mode extremal material presented in [47].

Mechanically, this architectured material carries an effective orthotropic behaviour (provided that the base material is isotropic [48]). Assuming an a-priori linear elastic behaviour

implies that four independent coefficients need to be identified, namely one (respectively two) effective Young's modulus, two (respectively one) effective Poisson's ratios and the effective shear modulus. The theoretical values of the Poisson's ratios in [36] are $\nu_{12}^H = -1.25$ and $\nu_{21}^H = -0.4$. The complete effective tensor $\mathbb{C}^H$ is provided in Appendix A alongside a discussion on both the elastic behaviour of the unit cell at small strain and the identification of effective elastic coefficients.

The choice to demonstrate our procedure on this specific micro-structure is motivated by several reasons. First, this shape is an auxetic material with micro-structural deformation mechanisms, which makes it a candidate to be studied using multi-scale approach. Second, its orthotropic behaviour is the most generic state that can be achieved when designing composites with single base material. Third, this architectured material is amenable to large strain analyses.

2.2. Fabrication of natural rubber architectured sheets

We fabricated three sorts of specimens consisting of periodic assemblages of the unit cell: two specimens designed for uniaxial tension along directions $\boldsymbol{e_1}$ and $\boldsymbol{e_2}$, hereafter referred to as specimens T_1 and T_2 respectively, and one specimen designed for a simple shear test, hereafter referred to as specimen S. The periodic array for each sample is set at:

- 5×8 unit cells for the tensile specimen T_1 (see Figure 2(b)),
- 8×5 unit cells for the tensile specimen T_2,
- a sequence of two lattices of 8×5 unit cells for the shear specimen S (see Figure 2(c)). The arrangement is made to balance the torques.

For all specimens, the size of the square unit cell was set at 10 mm × 10 mm, yielding a 50 mm × 80 mm lattice. The generated pattern is then completed by 50 mm × 10 mm rectangular solid tabs that permit the clamping to the uniaxial testing machine. The specimens are laser cut from a 1.5 mm-thick natural rubber sheet with a Universal ILS9 120 W laser cutter (single cut at 35% power and 5% speed). To avoid burning the rubber, the machine blows compressed air onto the part being cut. Prior to applying the speckle pattern on the specimens, these are thoroughly washed with standard dish-washing soap.

2.3. Experimental setup and testing

To provide a complete characterization of the selected geometry, the evolving pattern transformations are investigated through uniaxial tensile and simple shear tests, as shown in Figure 2(b,c). The experiments are conducted under displacement control at a quasi-static strain rate $\dot{\varepsilon} = 0.125\,\mathrm{min}^{-1}$ up to 0.5 effective engineering strain for the tensile test and up to 0.45 effective engineering strain for the shear case. The tests are performed on an Instron 10 kN universal testing machine, with a mounted 50 N load cell ensuring accurate measurements down to ±0.1 N. The specimens are clamped at both ends with metallic bars, to constrain their displacement (see Figure 2(b)). The choice of hard clamp, which yield a strain heterogeneity in the specimens, was merely intended to facilitate the description of

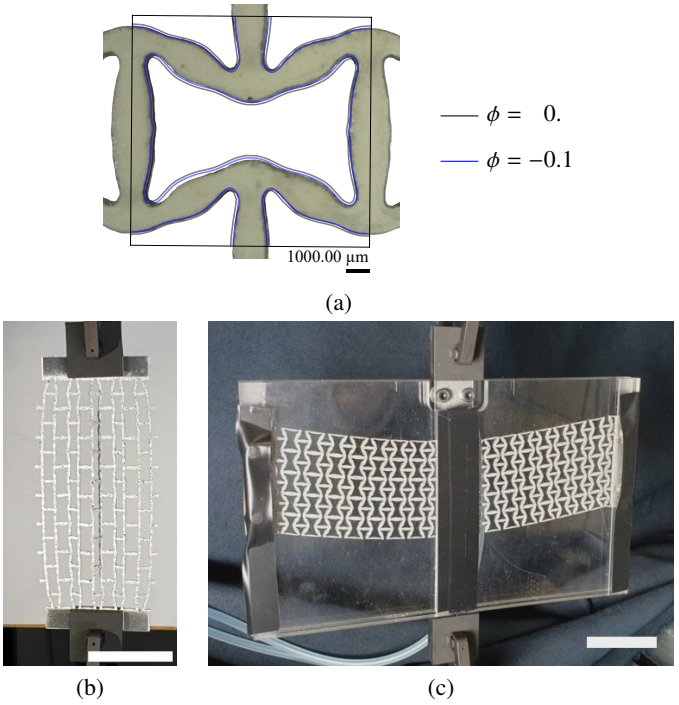

Figure 2: (a) View of a unit cell of the fabricated specimen under a Keyence VHX-1000 optical microscope. (b-c) Setup for the tensile test (specimen T_1 here) and shear test (specimen S). In the shear test, PMMA confining plates are held together at their edges and are attached to the (sliding) upper grip. Conversely, the central rectangular rod is attached to the (fixed) lower grip. Scale bar is 40 mm.

the boundary conditions in the numerical simulations. Recent works in the literature [49] attempted to apply less constraining boundary conditions using rings and networks ensuring a homogeneous state of strain, at the cost of higher uncertainties on boundary conditions and stress state. For the shear test, a specific setup shown in Figure 2(c) a specific setup is designed to arrange the specimen in the tensile machine. PMMA confining plates, preventing out-of-plane displacement, are held together at their edges and are attached to the (sliding) upper grip. Conversely, the central rectangular rod is attached to the (fixed) lower grip. The experiments were piloted using the Instron BlueHill software. Each mechanical test was recorded and used for full-field measurements by Digital Image Correlation (DIC). The recordings were obtained using a high-resolution digital camera (JAI Spark SP-20000-USB camera with a resolution of 5120×3840 pixels equipped with a Tokina AT-X Pro 100 mm F2.8 macro lens), mounted on a perpendicular axis with respect to the plane of the specimen. To improve the precision of the measurements, a gray scale speckle pattern was placed on the sample by aerosol spray. Using an in-built computer program, 8-bit gray scale sub-images were stored every second during the loading, with a resolution of 5064×2438 pixels for the tensile tests and resolution of 2292×2488 pixels for the shear test (the resolution for the shear is approximately two times smaller than in the tensile test because the camera was installed to record the whole specimen, yet only half of the specimen is useful for the observations).

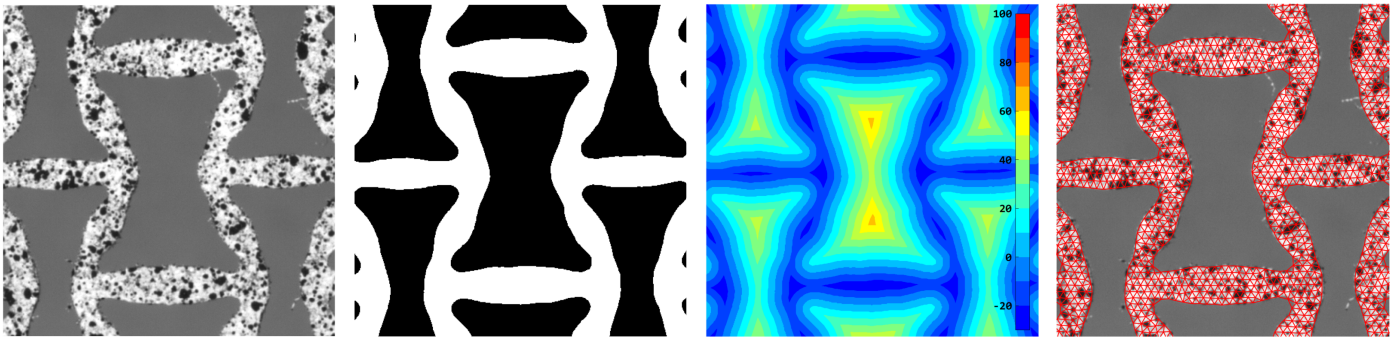

(a) Reference image (b) Binary mask (c) Signed distance in pixels (d) Final mesh

Figure 3: Procedure implemented to build the *experimental* meshes $\mathcal{M}^{DIC}$. From the reference acquired image of the specimen (a), a binary mask (b) is obtained by thresholding and median filtering. Then the distance transform of the mask is computed, and the obtained signed distance function (c) is used to build the triangulation with a uniform edge length [50].

2.4. Local and global Digital Image Correlation

All the experimental results shown in this work make use of the the Digital Image Correlation technique (DIC) to extract the structure motion from acquired images during the test. DIC procedures are based on the comparison of subsequent pictures of the structure [51]: given a *reference* image G and a *current* image g, the problem consists in finding the displacement field $\boldsymbol{u}(\boldsymbol{X})$ which minimizes the differences between the two images over the *Region Of Interst* $\mathcal{D}$ (ROI). The choices of the parametrization of the trial displacement field $\boldsymbol{u}(X)$ and the domain $\mathcal{D}$ are the main elements that distinguish: (i) the *local* approach [52], where $\mathcal{D}$ is divided into small sub-domains over which the displacement is assumed to be homogeneous, i.e. $\boldsymbol{u}(\boldsymbol{X}) = \boldsymbol{U}$ and (ii) the *global* approach [53, 54] where the displacement is defined over a finite-elements mesh covering the full ROI $\mathcal{D}$ (i.e $\boldsymbol{u}(\boldsymbol{X}) = \boldsymbol{N}(\boldsymbol{X}) \cdot \{\boldsymbol{u}\}$ with $\boldsymbol{N}(\boldsymbol{X})$ containing the finite element shape functions and $\{\boldsymbol{u}\}$ the nodal displacements to be determined). More details about the theoretical background and implementation are given in Appendix B.

While the comparison between both approaches in terms of efficiency and accuracy is still a hot topic in the community [55, 56], they are both used for different purposes in the present study. Indeed, the global approach assumes the displacement field continuity over the domain $\mathcal{D}$, which is well suited for the study of the structure at the *microscopic* scale (corresponding to the material continuum). Conversely, the local approach is employed to follow the motion of features associated to the *macroscopic* scale (corresponding to the pattern periodicity), for example to study the motion of the corner nodes of each unit cell.

All DIC results presented in this paper are obtained from an in-house academic code written by means of MATLAB scripts. For the global approach, linear triangular elements are used for meshing. The meshes are generated following the steps illustrated in Figure 3. Starting from the reference image (*i.e.* where the specimen is unstrained), a binary mask is obtained employing median filtering and gray level thresholding. The distance transform of the mask is then computed to obtain the *experimental* signed distance function from the specimen boundaries (see Figure 3(c)). Finally, the mesh of the specimen is generated using the `DistMesh` procedure proposed by Persson [50] from the obtained signed distance function. A uniform edge length of 12 pixels is chosen to correctly capture the localization of strains in the structure, while keeping a good DIC resolution (sub-pixel accuracy). Hereafter, the resulting mesh is referred as to $\mathcal{M}_i^{DIC}$ (i denotes the specimen name).

Theoretical background and implementation details associated to the DIC procedure are reported in Appendix B. For both local or global formulations, the DIC is performed iteratively following a Newton-Raphson procedure. The resulting displacement update (equation (B.7)) is used as the convergence criterion (equation (B.12)): the minimization is stopped when the maximum displacement step is below $\delta = 10^{-3}$ pixels (corresponding to a strain step of approximately 10^{-4} given the chosen edge length).

2.5. Numerical Simulations

Finite element method implementation. Finite element computations are undertaken under the assumption of large strains plane stress using the finite element solver Cast3M 2020 (`www-cast3m.cea.fr`). In the simulations, the conditions of the mechanical tests are exactly reproduced, *e.g.* the sample is loaded in with a prescribed displacement at the two ends. In both cases, the specimen is meshed with $P2$ triangle elements. The geometry of the specimen used for the computations is obtained following two strategies:

- from the *theoretical* level set function ϕ, using image processing to detect and extract the 0-level contour image of the level set function. Hereafter this mesh is referred as to $\mathcal{M}_i^{\phi=0}$ (i denotes the specimen name). For all specimens, the total numbers of elements and nodes are 80,000 and 171,534, respectively. $\mathcal{M}^{\phi=0}$ is perfectly periodic, *i.e.* it does not embed any geometrical defects;
- from the *experimental* mesh $\mathcal{M}_i^{DIC}$ (used for the global DIC presented in section 2.4). The total numbers of elements and nodes for the FE model are 78,380 and 166,982, respectively. By comparison to the theoretical mesh $\mathcal{M}_i^{\phi=0}$, $\mathcal{M}_i^{DIC}$ captures several geometrical imperfections induced by the fabri-

cation process and by the positioning of the specimen in the tensile machine.

Rubber material models. The constitutive behaviour of natural rubber is modelled as an incompressible hyperelastic material. Let $\boldsymbol{F} = \frac{\partial \boldsymbol{x}}{\partial \boldsymbol{X}}$ denote the deformation gradient mapping a material point from the reference position $\boldsymbol{X}$ to its current location $\boldsymbol{x}$. We adopt the Mooney-Rivlin model [57, 58], which is normally acceptable for intermediate elongations, *i.e.* between 50 -100%. The strain energy function of Mooney-Rivlin hyperelastic constitutive law is expressed as a function of strain invariants I_1, I_2, $I_3 = J^2$ of the left Cauchy-Green tensor $\boldsymbol{B} = \boldsymbol{F}\boldsymbol{F}^T$. The strain energy density function takes the form:

$$W = C_{10}(I_1 - 3) + C_{01}(I_2 - 3) + \frac{1}{d}(J-1)^2 \tag{2.1}$$

where C_{10}, C_{01} and d are material parameters. For the case of an incompressible Mooney-Rivlin material under uniaxial elongation, $\lambda_1 = \lambda$ and $\lambda_2 = \lambda_3 = 1/\sqrt{\lambda}$. Then the true stress (Cauchy stress) differences can be calculated as:

$$\begin{aligned} \sigma_{11} - \sigma_{33} &= 2C_{10}(\lambda^2 - \frac{1}{\lambda}) - 2C_{01}(\frac{1}{\lambda^2} - \lambda^2) \\ \sigma_{22} - \sigma_{33} &= 0 \end{aligned} \tag{2.2}$$

In the case of simple tension, $\sigma_{22} = \sigma_{33} = 0$. Then we can write:

$$\sigma_{11} = \left(2C_{10} + \frac{2C_{01}}{\lambda}\right)\left(\lambda^2 - \frac{1}{\lambda}\right) \tag{2.3}$$

and the engineering stress (force per unit reference area) for an incompressible MooneyRivlin material under simple tension can be calculated using $\sigma_{11}^{\text{eng}} = \sigma_{11}\lambda_2\lambda_3 = \sigma_{11}/\lambda = \sigma_{11}/(1 + e_{11}^{\text{eng}})$. Hence:

$$\begin{aligned} \sigma_{11}^{\text{eng}} &= \left(2C_{10} + \frac{2C_{01}}{\lambda}\right)\left(\lambda - \lambda^{-2}\right) \\ \sigma_{11}^{\text{eng}} &= \left(2C_{10} + \frac{2C_{01}}{1 + e_{11}^{\text{eng}}}\right)\left(1 + e_{11}^{\text{eng}} - \frac{1}{(1 + e_{11}^{\text{eng}})^2}\right) \end{aligned} \tag{2.4}$$

3. Results and discussion

3.1. Numerical simulations

Calibration of material parameters. The mechanical behaviour of natural rubber is identified from uniaxial tensile tests. Dogbone specimens are fabricated using a cutting die to make specimens for uniaxial tension (the dimensions of test specimens are depicted on Figure 4(a)) and are subjected to the uniaxial tensile tests with a speed of 10 mm/min. The measured engineering stressstrain response is shown in Figure 4(b). It is shown that the Mooney-Rivlin model is suitable to capture the tensile behaviour well up to 0.5 engineering strain for this natural rubber. The material coefficients $C_{10} = 0.199169$ MPa and $C_{01} = 0.134212$ MPa in the Mooney-Rivlin model for this natural rubber are identified by a non-linear fit from the experimental data.

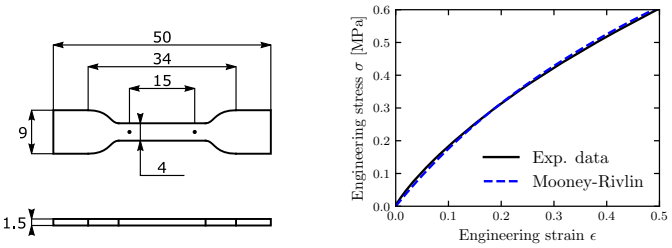

(a) (b)

Figure 4: (a) The dogbone geometry with its dimensions in mm. (b) Measured engineering stress-strain response under uniaxial tension. The Mooney-Rivlin hyperelastic model is employed to fit the stressstrain response and calibrate material parameters.

Shape sensitivity analysis. We first report the measured engineering stress-strain curves for all tests (see Figure 5). For tensile tests (specimens T_1 and T_2), the experiments are juxtaposed to the numerical results (for the shear, the frictions in the setup hinder an experimental estimate of the load.) Figure 5(b) and even more Figure 5(c-d) reveal a significant gap in stiffness between the numerical predictions on the theoretical mesh $\mathcal{M}^{\phi=0}$ (stiffest dashed gray curve) and on the experimental mesh $\mathcal{M}^{DIC}$. The latter model is in better agreement with the experiments (black curves). The strong differences between the two approaches in the numerical analyses suggest that the material effective stiffness is highly sensitive to the shape uncertainties induced during the laser cutting. To analyse the sensitivity of the mechanical behaviour to shape uncertainty, additional numerical simulations are carried out using *eroded* theoretical meshes, *i.e.* by progressively reducing the size of the trusses. In practice, we operate an erosion of the contour by introducing a negative offset to the signed distance function ϕ of Figure 1(a). The shapes for offsets varying between -0.1 and 0. with a step of 0.02 is shown in Figure 5(a). The experimental stress-strain curves of specimen T_2 (Figure 5(c)) are most similar to the eroded model with the level set shifted by -0.06. Using the properties of the signed distance function ϕ, the experimental specimen is expected to be fabricated with trusses that are roughly $120\,\mu$m thinner than expected. This gap to the laser cutting process. In hindsight, observing the specimens under an optical microscope (see Figure 2(a)) confirms that these are thinner than expected and also reveals that the error on the thickness is not constant along the trusses. In the following, the simulations performed on the experimental mesh $\mathcal{M}^{DIC}$ are used for the comparison with experiments and general validation.

3.2. Two-scale kinematic analysis

Scale of the sheet material continuum. For all the tests, the acquired images of the structure are reported in Figure 6 for stages corresponding to 0, 0.15, 0.3 and 0.45 engineering strain. The principal stretch field λ_1 resulting from the global-DIC procedure performed on a full set of acquired pictures is superimposed to the images. Following the procedure described in section 2.4, the *experimental* mesh $\mathcal{M}^{DIC}$ used to perform the DIC is defined at the reference stage. The obtained displacements

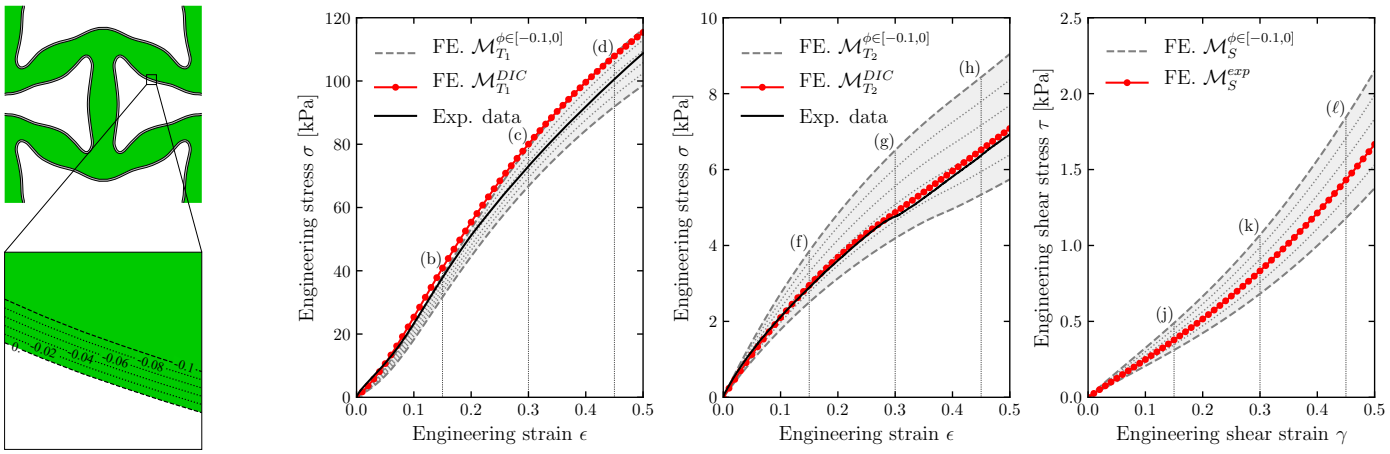

(a) Cut levels for ϕ (b) T_1 (c) T_2 (d) S

Figure 5: (a) Unit cell contour defined by the level set function ϕ with varying cutting heights. (b-d) Effective stress-strain curves for the structure. Comparison between experiments and numerical simulations with the Mooney-Rivlin hyperelastic model. The shaded gray areas encompass the stress-strain curves for $\phi \in [-0.1, 0]$. The letters appearing at 0.15, 0.3 and 0.45 effective strains refer to the deformed shapes in Figure 6.

fields permit a further comparison with predictions and give an insight on the deformation mechanism of the samples, *i.e.* how the structure moves and deforms.

In all the tests, the distribution of the elongation (Figure 6) obtained from the displacement field in both full-field measurement indicates that the strain field is mostly concentrated on the hinges of the structure. This emphasizes the predominance of structural deformation at small strain, where different parts of the *lattice* behave as rigid struts and deformable hinges, in spite of the soft natural rubber. For the tensile tests, a lateral expansion indicating a negative Poisson's ratio is visible in both T_1 and T_2 specimens. Despite these general observations, some discrepancies can be noticed between the two tensile specimens. First, the amount of transverse strain is obviously different between specimen T_1 and T_2, expressing the orthotropic nature of the design. Second, while the most of strain is localised at the hinge regions in the specimens T_2 and S, a clear elongation of the members is identified on specimen T_1.

Figure 6(b-d) shows that specimen T_1 undergoes a positive strain in the trusses under tension (at 0.15 effective strain, $\lambda_1 \approx 1.15$ in green), whereas the perpendicular members exhibit negative strain (with $\lambda_1 < 1$). This transverse compressive state is responsible for an out-of-plane buckling at ~ 0.15 effective engineering strain. Beyond this stage, a wrinkling deformation is observed *i.e.* each transverse branch becomes corrugated (see the central unit cells in Figure 2(b), Figure 6(c-d) and Movie 1). This particular instability is typical of the clamped boundary conditions imposed on the specimen, responsible for compressive stresses that develop in the transverse direction [59]. The buckling and post-buckling modelling, beyond the scope of the paper, is neither accounted nor permitted in the two-dimensional finite element model. Since DIC measurement is also based on a 2-d model, the out of plane deformation appears as compression state in the stretch field in Figure 6(c,d). Looking at Figure 5(b), this illustrates why the numerical simulation (curve in red) perfectly matches the experiment (curve in black) until 0.15 effective engineering strain, while it tends to overestimate the effective stress at larger strains. The maximal relative error between the experiment and the simulation is of 9.5%.

Specimen T_2 remains mostly unstrained at the core of the trusses throughout the test ($\lambda_1 \approx 1.$ in blue). The specimen remained in the plane during the whole test. However, unit cells located at its edges experienced snap-through instabilities just before 0.3 effective engineering strain. Indeed, the buckled cells that were almost unstrained in Figure 6(f) become the most strained in Figure 6(g,h). The full movie of the tensile test provided in the supplementary material permits to better appreciate the effect (see Movie 2). This effect is observed in both the experiments and the numerical simulations. This feature is also detected in Figure 5(b) where a local change in the slope of the stress-strain curve corresponding to the relaxation of the center cells accompanying the edge cells snap-through is identified. Note that the samples are *monostable* unlike the examples of [1], *i.e.* once unloaded, the specimens return to their initial configurations. In Figure 5(c), the numerical simulation (curve in red) correctly matches the experiment (curve in black) until 0.5 effective engineering strain. The small gap that appears around 0.3 effective engineering strain is attributed to the snapping effect which is not captured the numerical stress-strain curve. The maximal relative error between the experiment and the simulation is of 3%.

Regarding the shear test, specimen S is mounted horizontally (refer to Figure 2(b)). Therefore, its own weight induces an initial bending visible in Figure 6(i). Nonetheless, the role of the weight rapidly becomes negligible as the applied shear load increases ($\gamma > 0.1$). As we establish a relative good agreement between simulation and experiments under uniaxial tension (besides structural instabilities that were not accounted), the finite element method permits to estimate the stress distribution during shear test (see Figure 5(d)). The maximal effective shear stress τ computed numerically is around 1.75 kPa,

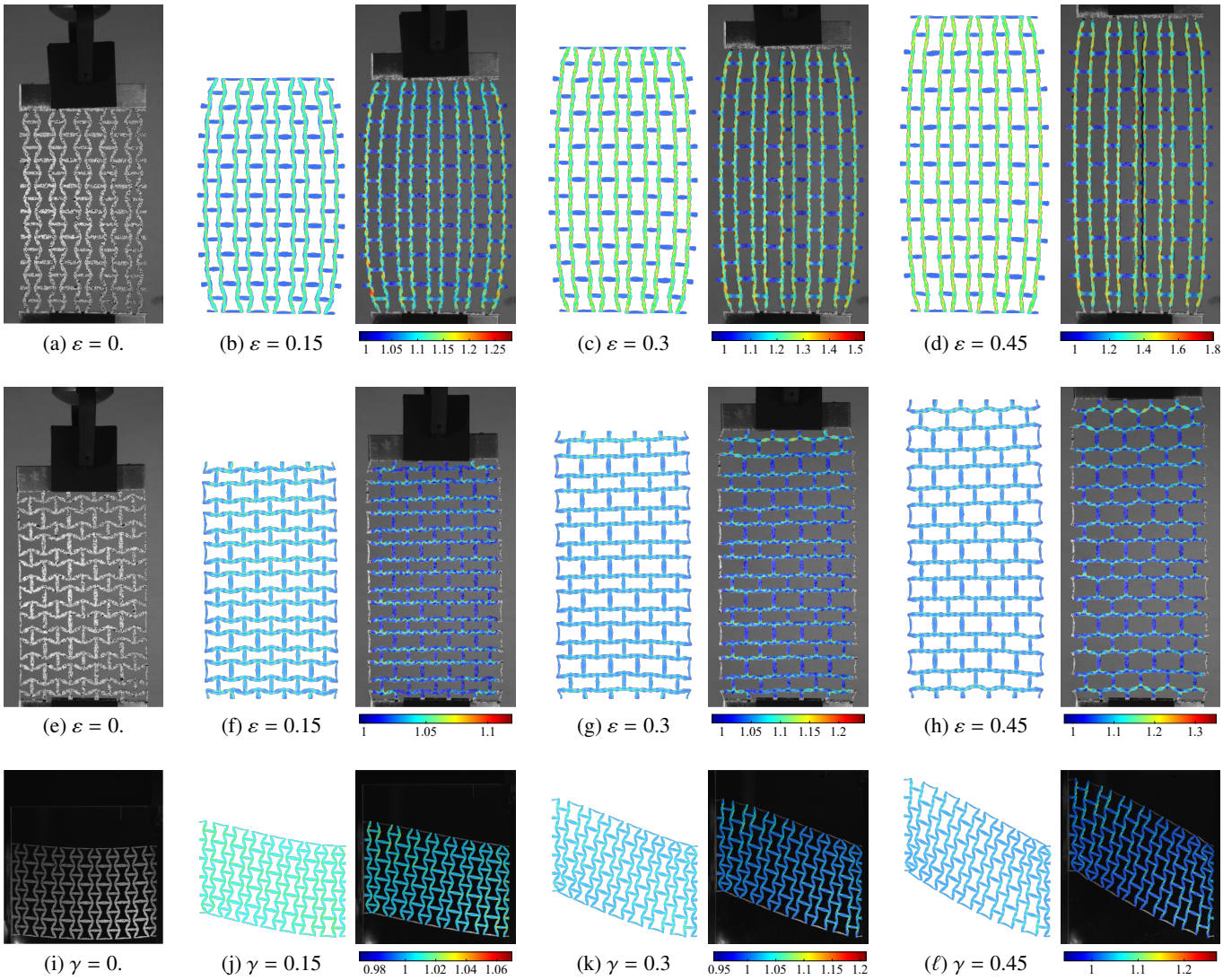

Figure 6: Numerical and experimental deformed configurations of specimens T_1 (a-d), T_2 (e-h) and S (i-ℓ) at different levels of imposed engineering effective strain: $0, 0.15, 0.30$ and 0.45. The principal stretch λ_1 is plotted as a colour map in each figure. The colour bar is the same for both the numerical and experimental results.

yielding a resultant load of 0.14N. Note that experimentally, a nearly constant force of 3.5N was measured, mostly indebted to frictional forces in the setup holding the specimen. Since the contributions of the specimen response and the frictional forces could not be separated in the measured load, no experimental load values could be provided for the shear specimen. Moving on to the deformed of the specimen S, we remark, more than in any other tests of the present work, a strong heterogeneity in the strain field. Rather than experiencing a homogeneous shear, the specimen S undergoes rotations, leaving zones with predominant tension (top left and bottom right of S, see Figure 6(k-ℓ)), predominant compression (top right and bottom left of S), and predominant shear (at the center of S). These observations will be developed in the next paragraphs.

Scale of the unit cell. Next, we intend to analyse the global kinematics of the material, *i.e.* the averaged kinematic values over the unit cells. To this end, we perform a local-DIC measurement for all the tests. We measure the macroscopic displacement at each node of the lattice, and derive the strain field, depicted in Figure 7. In particular, Figure 7(a,e) illustrate the evolution of the averaged transverse strain with respect to the averaged longitudinal strain for all unit cells of the specimens. The ratio of the averaged strain components (*i.e.* the slope of the curves) yields the effective Poisson's ratios, ν_{12} and ν_{21} respectively.

At finite strains, the mechanical behaviour shifts rapidly, indicating in particular a decrease of the "auxeticity" of the specimen. Beyond 10% effective strain, both effective Poisson's ratios no longer satisfy the small strain prediction of [36] (reported also in Appendix A). This effect is known in re-entrant honeycombs: the evolution of the Poisson's ratio with applied strain has already been observed and discussed in [60]. Note also that improvements in the design of re-entrant honeycombs using a non-linear material behaviour in the optimization process would permit to stabilize the Poisson's ratio in a range up to 0.2 engineering strain, as shown in [28].

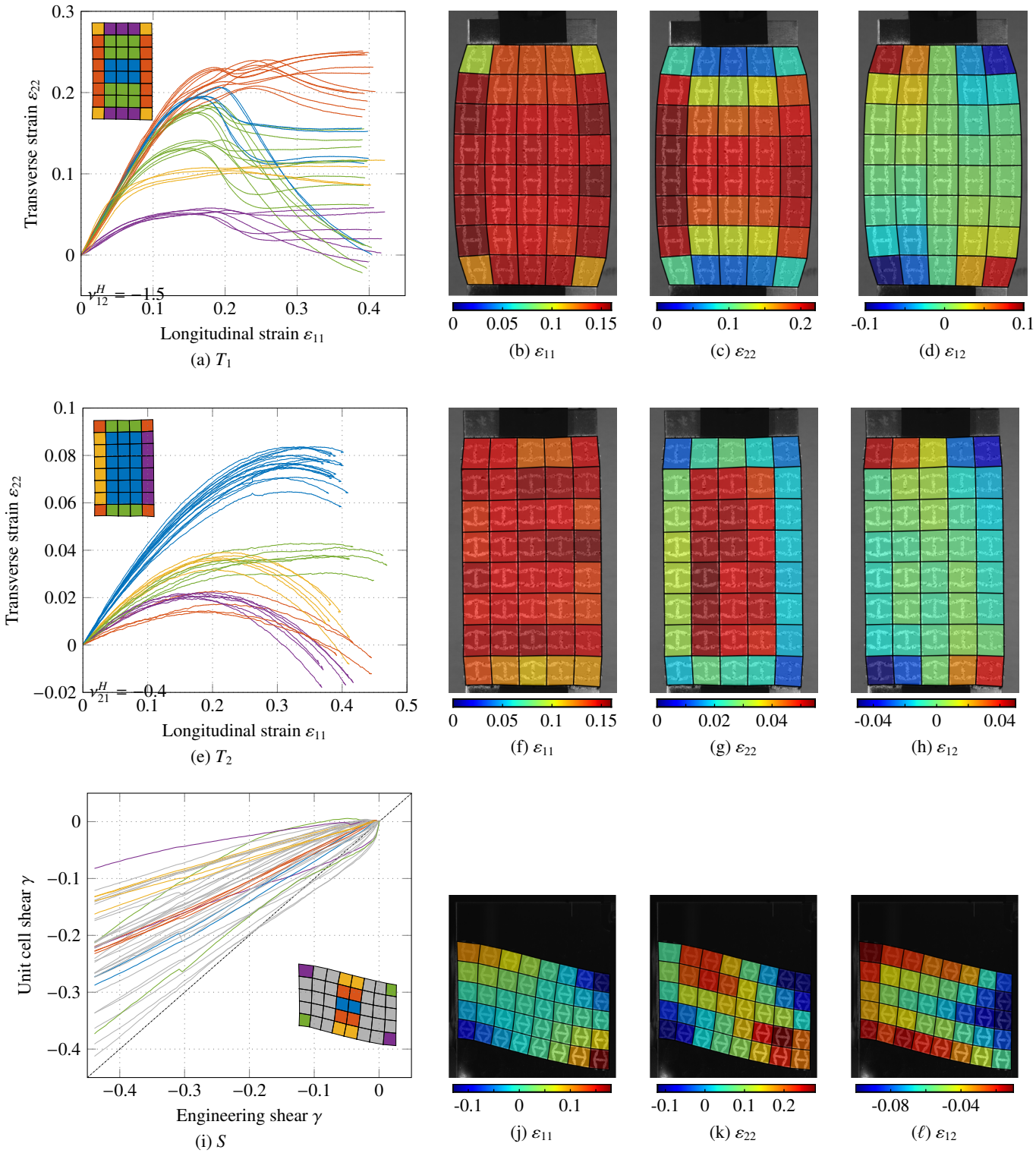

Figure 7: Evolution of the macroscopic transverse strain ε_{22} with respect to the longitudinal strain ε_{11} for specimen T_1 (a) and specimen T_2 (e). Evolution of the macroscopic shear strain ε_{12} with respect to the effective engineering shear strain γ for specimen S (i). The behaviour of the unit cells can be regrouped in bundles represented by different colours. Macroscopic strains maps obtained via *local* DIC at a loading stage of 0.15 engineering strain, (b-d) for specimen T_1 ; (f-h) for specimen T_2 ; (j-ℓ) for specimen S.

Strain heterogeneity in the specimen. We further explore the strain heterogeneity in the specimen. The question has an importance in itself, as mathematical optimisation methods are generally defined on unit cells with periodic boundary conditions. Indeed, the interest is often on the *macroscopic* behaviour of the structure, hence considered as a continuum material with *homogenized* properties. The computation of this macroscopic apparent behaviour from the microscopic unit cell configuration (geometry and material properties) uses the assumption of an homogeneous state of strain in the structure [48], equivalent to considering a specimen of infinite size. However, the specimen size is in practice limited by the experimental setup. As a consequence, boundary conditions applied to the specimen (free surfaces, clamping, etc.) are the source of strain heterogeneities.

In all the tests, the macroscopic behaviour of the cells can be regrouped in *bundles*, identified by curves with different colours in Figure 7(a,e,i). The scatter of the bundles is a evidence of heterogeneity in the specimen.

For specimen T_2 (see Figure 7(e)), there is merely a single line of cells which is affected by the boundary conditions, generally showing a lower transverse strain than center cells: cells associated to the clamped boundaries (in green and yellow) are constrained kinematically, while cells located on free edges (orange ad purple) are less strained transversely because of the vanishing transverse stresses. Apart from this boundary layer, the cells in the center of the specimen belong to the same bundle (coloured in blue), thus denoting a uniform state of strain in this region. Hence, the observed cell behaviour can be expected to be close to the homogenised behaviour; this is verified with the macroscopic Poisson's ratio identified close to the theoretical value of $\nu_{21}^H = -0.4$ (dash-dot black line).

By opposition, the specimen T_1 (see Figure 7(a)) shows an highly heterogeneous state of strain, with cell bundles that are more difficult to separate. This is mainly due to the higher absolute value of the Poisson's ratio ($\nu_{12}^H \approx -1.5$, dash-dot black line). At small strain *i.e.* between 0 and 0.05 effective engineering strain, the specimen is rather homogeneous (besides the purple bundles, the unit cells all follow the same trend). Between 0.05 and 0.15, each bundle sequentially start to behave independently (yellow bundle, then green bundle, orange bundle, etc.). To better appreciate the average strain distribution in the specimen, A video of the test with the superimposed averaged strain field is provided (see Movie 3). We remark that at 0.15 effective engineering strain, we need three lines of cells from the constrained zones to neglect the influence of the boundary conditions. Hence, only the two central lines of the specimen are not affected by the boundary conditions (see Figure 7(c)).

Regarding the shear specimen S (see Figure 6(i- ℓ)), we notice that the unit cells shear strain γ is in general lower than the engineering shear γ_S imposed on the specimen. This is mostly due to the rotation of cells in the center region. In addition, a shear strain gradient is observed in the specimen, with a higher value in the center cells (in blue) that decreases with approaching boundaries (orange and yellow); this is in agreement with the free edge condition at which the shear stresses vanish. Moreover, the corner cells can be separated in two cases. First, bottom-left and top-right cells, in green, are first compressed in the early stages up to a point where contact occurs between members ($\gamma_S \approx 15\%$); then these cells are submitted to more shear in the latter stages. Second, top-left and bottom-right cells, in purple, are mostly stretched because of the specimen curvature. Despite the observed strain heterogeneity, it can be seen that the two center cells in blue are loaded proportionally to the imposed shear (with $\gamma \approx 0.65\gamma_S$).

3.3. Truss-hinge equivalent kinematic model

Since the strain distribution of specimen T_2 is localized at the hinges of the structure, we examine whether a simple kinematic model with rigid trusses and rotating hinges (nodes) is sufficient to predict the Poisson's ratio of the structure. To this end, we derive a generic parametrization of the unit cell of Figure 1 based upon its morphological *skeleton*, which is a "wire" version of the shape that is equidistant to its boundaries. In shape ahnalysis, the *skeleton* is frequently used as shape descriptors as it usually emphasizes geometrical and topological properties of the shape, such as its connectivity, topology, length, direction, and width. Interested readers may refer to [61, 62] for a mathematical definition of skeletons and algorithms to compute them. In our work, the morphological skeleton of our architecture is computed from a rasterized binary version of Figure 1 via the `SkeletonTransform` command from Wolfram Mathematica (version 11.2, 2018). The obtained result is depicted in Figure 8(a,b) (geometry in black, that was duplicated for a better distinction with the models). We remark that in spite of the relative complexity of the cell geometry, the corresponding skeleton can be approximated by a couple of straight features (beams) and nodes connecting them (hinges), arranged like in a simple re-entrant honeycomb. In particular, two configurations are easily derivable from the skeleton:

- configuration $\mathcal{K}_{beams}$ (depicted in blue in Figure 8(a)) is meant to emphasize the arrangement of the principal beams at the expense of the nodes position. The identification of the beams is easily achieved through a linear fit. The `ImageLines` command from Wolfram Mathematica finds line segments of a rasterized binary image and returns the coordinates of their endpoints. This configuration presumably yields the *smallest* angle between trusses θ.

- configuration $\mathcal{K}_{nodes}$ (depicted in orange in Figure 8(a)) is meant to emphasize the position of the nodes. The identification of the nodes is done manually on the skeleton. This configuration presumably yields the *largest* angle between trusses θ.

Naturally, the real configuration may stand between $\mathcal{K}_{beams}$ and $\mathcal{K}_{nodes}$. This configuration should accurately predict the evolution of the effective transverse strain ε_{22} with respect to the effective longitudinal strain ε_{11} observed experimentally. We define it to reproduce as accurately as possible the experimental behaviour:

- configuration $\mathcal{K}_{ls}$ is obtained by finding the angle θ which best fits the experimental experimental curve $\varepsilon_{22} = f(\varepsilon_{11})$. We use the least square method to find the best angle θ that fits the experimental curve.

Given the equivalent truss-hinge model, we understand the whole unit cell kinematics are merely driven by the only variable angle θ, therefore strain components can be expressed as:

$$\begin{aligned} \text{Longitudinal:} \quad & \epsilon_{22}(\theta) = \frac{2e}{L}\left(\cos(\theta_0) - \cos(\theta)\right) \\ \text{Transverse:} \quad & \epsilon_{11}(\theta) = \frac{\sin(\theta)}{\sin(\theta_0)} - 1 \end{aligned} \tag{3.1}$$

where L is the characteristic length of the unit cell and θ_0 denotes the initial value of θ (when the structure has not been stretched yet).

Starting from the images of specimen T_2 recorded during the tensile test, we compute the morphological skeleton of the central unit cell and inferred a measure of the angle θ considering both $\mathcal{K}_{beams}$ and $\mathcal{K}_{nodes}$. The evolution of θ measured during the experiments is compared to the rigid trusses rotating hinges model (see equation (3.1)) in Figure 8(b) for both $\mathcal{K}_{beams}$ and $\mathcal{K}_{nodes}$. We remark that configuration $\mathcal{K}_{nodes}$ yield excellent agreement between model and experiments. Conversely, the model using configuration $\mathcal{K}_{beams}$ tends to underestimate the experiments.

Next, we plot the evolution of the transverse strain with respect to the longitudinal strain (Figure 8(c)) at the scale of the unit cell. We remark that the experimental evolution, obtained previously in Figure 7(e), is bounded between the predictions of the two analytical models assuming $\mathcal{K}_{beams}$ and $\mathcal{K}_{nodes}$. Using the least square method, we obtain that theoretical kinematic evolution (equation (3.1)) best approximates the experiments (curve in black) assuming an intial angle $\theta_0 = 68°$. This configuration corresponds to $\mathcal{K}_{ls}$. Remarkably, the results for $\mathcal{K}_{ls}$ (dashed green curve) are in excellent agreement with the experiments, despite the simplicity of the model. It is also worth noting that the $\theta_0 = 68°$ case fits particularly well the end of the experimental $\mathcal{K}_{beams}$ (continuous blue curve) in Figure 8(a). The obtained results support the idea that a rigid trusses rotating hinges kinematic model is suitable to predict the deformation pattern of specimen T_2 in spite of the soft elastomer used in the fabrication of the specimens.

4. Concluding remarks

In this work, we have introduced a multi-scale experimental analysis designed to completely characterize the behaviour of architectured sheets undergoing extreme deformation. Our techniques have been applied to the analysis of a soft, auxetic sheet subjected to large tensile and shear loads (up to 0.5 effective strain). Based on this analysis, we are able to:

- gain insight on the strain distribution of the specimen and identify the zones that have uniform strain field. This identification is particularly simple in our study, owing to our reconstruction of the macroscopic strain (the averaged kinematic values over each unit cell);

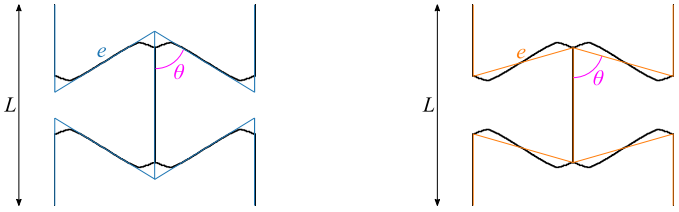

Exp. skeleton $\mathcal{K}_{beams}$ $\mathcal{K}_{nodes}$

Configuration	$\mathcal{K}_{beams}$	$\mathcal{K}_{nodes}$
e/L	0.58	0.52
θ_0	59°	74°

(a)

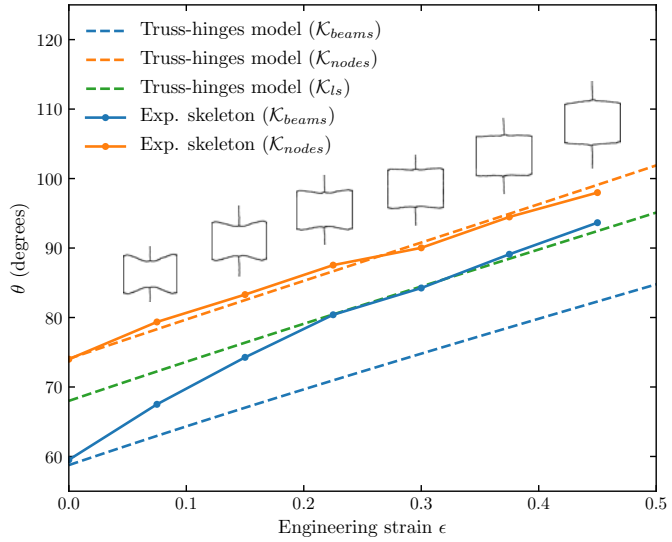

(c)

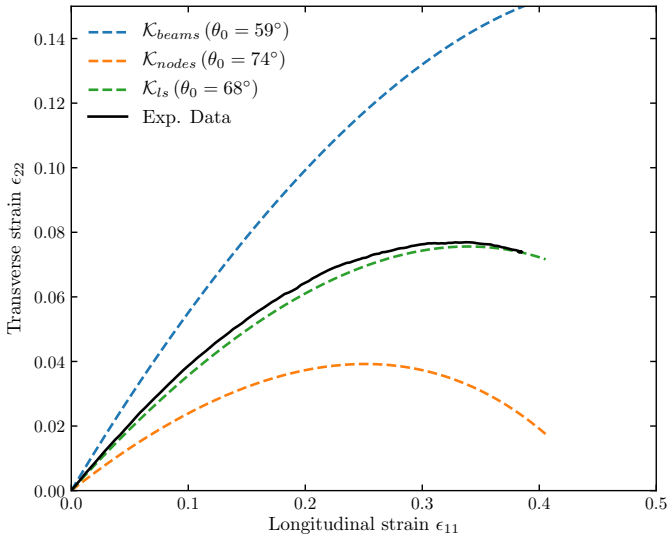

(d)

Figure 8: Truss-hinge model. (a) Parametrization assuming configuration $\mathcal{K}_{beams}$ (blue) and $\mathcal{K}_{nodes}$ (orange) superimposed to the skeleton of the unit cell (black). (c) and (d): corresponding kinematic data with both experimental values (continuous curves) and predictions from equation (3.1) (dashed curves). (c) Hinge aperture angle θ as a function of the effective engineering strain. Experimental data is identified from the pictures of the tensile tests at different strain levels. The skeletal representation of the central cell for various strain level are included.(d) Interdependence of the macroscopic strain components. The experimental curve is a mean of the blue bundle in Figure 7(e).

- determine that strain heterogeneities dominate the response of finite-size specimens and that, to accurately capture the tensile response of an infinite sheet, the number of unit cells should be greater than four in both horizontal and transverse directions;
- use the wealth of information obtained from the experiments to create a reduced order model (featuring rigid trusses and flexible hinges) that accurately describes the kinematic behaviour under tensile loads;
- determine that, despite the strong heterogeneity displayed by the shear test results, it is possible to identify zones in the center of the specimen where the shear state is proportional to the applied engineering shear strain.

As an outlook, the proposed procedures could benefit from a proper quantification of the errors associated to the identified data. This uncertainty analysis could be inspired from works already available in the literature [63–65]. The tools presented in this study can be readily adapted to any two-dimensional architectured solid undergoing small or large deformations [2, 33, 66]. In turn, the results that can be obtained by using these methods can potentially be leveraged to create tunable and stretchable mechanical devices [9, 11].

Acknowledgements

This work was partly financed by the french-swiss ANR-SNF project MechNanoTruss (ANR-15-CE29-0024-01). F.A. acknowledges the support of the French doctoral fellowship "Contrat Doctoral Spcifique pour Normalien". C.D. acknowledges support from the US Army Research Office Grant W911NF- 17-1-0147.

Additional information

Supplementary material is available for this paper.

- Movie 1: Green-Lagrange strain field obtained via *global* DIC at the center of specimen T_1;
- Movie 2: Principal stretch λ_1 field obtained via *global* DIC on specimen T_2;
- Movie 3: Macroscopic strains maps obtained via *local* DIC for specimen T_1.

[1] A. Rafsanjani, D. Pasini, Bistable auxetic mechanical metamaterials inspired by ancient geometric motifs, Extreme Mech. Lett. 9 (2016) 291–296. doi:10.1016/j.eml.2016.09.001.

[2] Y. Tang, J. Yin, Design of cut unit geometry in hierarchical kirigami-based auxetic metamaterials for high stretchability and compressibility, Extreme Mech. Lett. 12 (2017) 77–85. doi:10.1016/j.eml.2016.07.005.

[3] P. Celli, C. McMahan, B. Ramirez, A. Bauhofer, C. Naify, D. Hofmann, B. Audoly, C. Daraio, Shape-morphing architected sheets with non-periodic cut patterns, Soft Matter 14 (48) (2018) 9744–9749. doi:10.1039/c8sm02082e.

[4] J. Liu, Y. Zhang, Soft network materials with isotropic negative Poisson's ratios over large strains, Soft Matter 14 (5) (2018) 693–703. doi:10.1039/c7sm02052j.

[5] L. Malomo, J. Pérez, E. Iarussi, N. Pietroni, E. Miguel, P. Cignoni, B. Bickel, Flexmaps: Computational design of flat flexible shells for shaping 3D objects, ACM Trans. Graph. 37 (6) (2018) 1–14. doi:10.1145/3272127.3275076.

[6] G. P. T. Choi, L. H. Dudte, L. Mahadevan, Programming shape using kirigami tessellations, Nat. Mater. 18 (9) (2019) 999–1004. doi:10.1038/s41563-019-0452-y.

[7] J. W. Boley, W. M. van Rees, C. Lissandrello, M. N. Horenstein, R. L. Truby, A. Kotikian, J. A. Lewis, L. Mahadevan, Shape-shifting structured lattices via multimaterial 4d printing, Proc. Natl. Acad. Sci. U.S.A. 116 (42) (2019) 20856–20862. doi:10.1073/pnas.1908806116.

[8] R. Guseinov, C. McMahan, J. Pérez, C. Daraio, B. Bickel, Programming temporal morphing of self-actuated shells, Nat. Commun. 11 (1). doi:10.1038/s41467-019-14015-2.

[9] Y. Jiang, Z. Liu, N. Matsuhisa, D. Qi, W. R. Leow, H. Yang, J. Yu, G. Chen, Y. Liu, C. Wan, Z. Liu, X. Chen, Auxetic mechanical metamaterials to enhance sensitivity of stretchable strain sensors, Adv. Mater. 30 (12) (2018) 1706589. doi:10.1002/adma.201706589.

[10] Y. Wang, Q. Liu, J. Zhang, T. Hong, W. Sun, L. Tang, E. Arnold, Z. Suo, W. Hong, Z. Ren, C. F. Guo, Giant Poisson's effect for wrinkle-free stretchable transparent electrodes, Adv. Mater. 31 (35) (2019) 1902955. doi:10.1002/adma.201902955.

[11] Y.-J. Lee, S.-M. Lim, S.-M. Yi, J.-H. Lee, S. gyu Kang, G.-M. Choi, H. N. Han, J.-Y. Sun, I.-S. Choi, Y.-C. Joo, Auxetic elastomers: mechanically programmable meta-elastomers with an unusual Poisson's ratio overcome the gauge limit of a capacitive type strain sensor, Extreme Mech. Lett. 31 (2019) 100516. doi:10.1016/j.eml.2019.100516.

[12] M. N. Ali, J. J. C. Busfield, I. U. Rehman, Auxetic oesophageal stents: structure and mechanical properties, J. Mater. Sci.: Mater. Med. 25 (2) (2013) 527–553. doi:10.1007/s10856-013-5067-2.

[13] M. Kapnisi, C. Mansfield, C. Marijon, A. G. Guex, F. Perbellini, I. Bardi, E. J. Humphrey, J. L. Puetzer, D. Mawad, D. C. Koutsogeorgis, D. J. Stuckey, C. M. Terracciano, S. E. Harding, M. M. Stevens, Auxetic cardiac patches with tunable mechanical and conductive properties toward treating myocardial infarction, Adv. Funct. Mater. 28 (21) (2018) 1800618. doi:10.1002/adfm.201800618.

[14] O. Duncan, T. Shepherd, C. Moroney, L. Foster, P. Venkatraman, K. Winwood, T. Allen, A. Alderson, Review of auxetic materials for sports applications: expanding options in comfort and protection, Appl. Sci. 8 (6) (2018) 941. doi:10.3390/app8060941.

[15] L. Foster, P. Peketi, T. Allen, T. Senior, O. Duncan, A. Alderson, Application of auxetic foam in sports helmets, Appl. Sci. 8 (3) (2018) 354. doi:10.3390/app8030354.

[16] Z. Wang, H. Hu, Auxetic materials and their potential applications in textiles, Text. Res. J. 84 (15) (2014) 1600–1611. doi:10.1177/0040517512449051.

[17] M. Konaković, K. Crane, B. Deng, S. Bouaziz, D. Piker, M. Pauly, Beyond developable: Computational design and fabrication with auxetic materials, ACM Trans. Graph. 35 (4) (2016) 1–11. doi:10.1145/2897824.2925944.

[18] S. W. Pattinson, M. E. Huber, S. Kim, J. Lee, S. Grunsfeld, R. Roberts, G. Dreifus, C. Meier, L. Liu, N. Hogan, J. Hart, Additive manufacturing of biomechanically tailored meshes for compliant wearable and implantable devices, Adv. Funct. Mater. 29 (32) (2019) 1901815. doi:10.1002/adfm.201901815.

[19] G. Allaire, Shape Optimization by the Homogenization Method, Springer New York, 2002. doi:10.1007/978-1-4684-9286-6.

[20] M. P. Bendsøe, O. Sigmund, Topology Optimization, Springer Berlin Heidelberg, 2004. doi:10.1007/978-3-662-05086-6.

[21] Y. Wang, Z. Luo, N. Zhang, Z. Kang, Topological shape optimization of microstructural metamaterials using a level set method, Comput. Mater. Sci. 87 (2014) 178–186. doi:10.1016/j.commatsci.2014.02.006.

[22] P. Vogiatzis, S. Chen, X. Wang, T. Li, L. Wang, Topology optimization of multi-material negative Poisson's ratio metamaterials using a reconciled level set method, Comput. Aided Des. 83 (2017) 15–32. doi:10.1016/j.cad.2016.09.009.

[23] Z.-P. Wang, L. H. Poh, J. Dirrenberger, Y. Zhu, S. Forest, Isogeometric shape optimization of smoothed petal auxetic structures via computational periodic homogenization, Comput. Methods Appl. Mech. Eng. 323 (2017) 250–271. doi:10.1016/j.cma.2017.05.013.

[24] J. Gao, H. Li, Z. Luo, L. Gao, P. Li, Topology optimization

of micro-structured materials featured with the specific mechanical properties, Int. J. Comput. Methods (2018) 1850144doi:10.1142/s021987621850144x.

[25] G. Nika, A. Constantinescu, Design of multi-layer materials using inverse homogenization and a level set method, Comput. Methods Appl. Mech. Eng. 346 (2019) 388–409. doi:10.1016/j.cma.2018.11.029.

[26] F. Wang, O. Sigmund, J. S. Jensen, Design of materials with prescribed nonlinear properties, J. Mech. Phys. Solids 69 (2014) 156–174. doi:10.1016/j.jmps.2014.05.003.

[27] A. Clausen, F. Wang, J. S. Jensen, O. Sigmund, J. A. Lewis, Topology optimized architectures with programmable Poisson's ratio over large deformations, Adv. Mater. 27 (37) (2015) 5523–5527. doi:10.1002/adma.201502485.

[28] G. Zhang, K. Khandelwal, Computational design of finite strain auxetic metamaterials via topology optimization and nonlinear homogenization, Comput. Methods Appl. Mech. Eng. 356 (2019) 490–527. doi:10.1016/j.cma.2019.07.027.

[29] S. Tan, J. Gu, S. C. Han, D.-W. Lee, K. Kang, Design and fabrication of a non-clogging scaffold composed of semi-permeable membrane, Mater. Des. 142 (2018) 229–239. doi:10.1016/j.matdes.2018.01.033.

[30] R. L. Truby, J. A. Lewis, Printing soft matter in three dimensions, Nature 540 (7633) (2016) 371–378. doi:10.1038/nature21003.

[31] T. D. Ngo, A. Kashani, G. Imbalzano, K. T. Q. Nguyen, D. Hui, Additive manufacturing (3d printing): A review of materials, methods, applications and challenges, Compos. B. Eng. 143 (2018) 172–196. doi:10.1016/j.compositesb.2018.02.012.

[32] C. Coulais, A. Sabbadini, F. Vink, M. van Hecke, Multi-step self-guided pathways for shape-changing metamaterials, Nature 561 (7724) (2018) 512–515. doi:10.1038/s41586-018-0541-0.

[33] L. Mizzi, E. Salvati, A. Spaggiari, J.-C. Tan, A. M. Korsunsky, Highly stretchable two-dimensional auxetic metamaterial sheets fabricated via direct-laser cutting, Int. J. Mech. Sci. 167 (2020) 105242. doi:10.1016/j.ijmecsci.2019.105242.

[34] J. Marty, J. Rthor, A. Combescure, P. Chaudet, Finite strain kinematics of multi-scale material by digital image correlation, Exp. Mech. 55 (9) (2015) 1641–1656. doi:10.1007/s11340-015-0059-4.

[35] S. Shan, S. H. Kang, Z. Zhao, L. Fang, K. Bertoldi, Design of planar isotropic negative poisson's ratio structures, Extreme Mech. Lett. 4 (2015) 96–102. doi:10.1016/j.eml.2015.05.002.

[36] F. Agnelli, A. Constantinescu, G. Nika, Design and testing of 3d-printed micro-architectured polymer materials exhibiting a negative Poisson's ratio, Continuum Mech. Thermodyn. 32 (2) (2020) 433–449. doi:10.1007/s00161-019-00851-6.

[37] J. Rthor, C. Kaltenbrunner, T. B. T. Dang, P. Chaudet, M. Kuhn, Gradient-elasticity for honeycomb materials: validation and identification from full-field measurements, Int. J. Solids Struct. 72 (2015) 108–117. doi:10.1016/j.ijsolstr.2015.07.015.

[38] J. N. Grima, A. Alderson, K. E. Evans, Auxetic behaviour from rotating rigid units, Phys. Status Solidi B 242 (3) (2005) 561–575. doi:10.1002/pssb.200460376.

[39] M. Fu, O. Xu, L. Hu, T. Yu, Nonlinear shear modulus of re-entrant hexagonal honeycombs under large deformation, Int. J. Solids Struct. 80 (2016) 284–296. doi:10.1016/j.ijsolstr.2015.11.015.

[40] E.-H. Harkati, N. Daoudi, A. Bezazi, A. Haddad, F. Scarpa, In-plane elasticity of a multi re-entrant auxetic honeycomb, Compos. Struct. 180 (2017) 130–139. doi:10.1016/j.compstruct.2017.08.014.

[41] X. Liang, A. J. Crosby, Uniaxial stretching mechanics of cellular flexible metamaterials, Extreme Mech. Lett. 35 (2020) 100637. doi:10.1016/j.eml.2020.100637.

[42] S. D. Papka, S. C. Kyriakides, In-plane biaxial crushing of honeycombs—: Part ii: Analysis, Int. J. Solids Struct. 36 (29) (1999) 4397–4423. doi:10.1016/s0020-7683(98)00225-x.

[43] H. Qiu, Y. Li, T. F. Guo, X. Guo, S. Tang, Deformation and pattern transformation of porous soft solids under biaxial loading: experiments and simulations, Extreme Mech. Lett. 20 (2018) 81–90. doi:10.1016/j.eml.2018.01.008.

[44] Y. He, Y. Zhou, Z. Liu, K. M. Liew, Buckling and pattern transformation of modified periodic lattice structures, Extreme Mech. Lett. 22 (2018) 112–121. doi:10.1016/j.eml.2018.05.011.

[45] G. Allaire, F. Jouve, A.-M. Toader, Structural optimization using sensitivity analysis and a level-set method, J. Comput. Phys. 194 (1) (2004) 363–393. doi:10.1016/j.jcp.2003.09.032.

[46] X. Wang, Y. Mei, M. Y. Wang, Level-set method for design of multi-phase elastic and thermoelastic materials, Int. J. Mech. Mater. Des. 1 (3) (2004) 213–239. doi:10.1007/s10999-005-0221-8.

[47] G. W. Milton, A. V. Cherkaev, Which elasticity tensors are realizable?, J. Eng. Mater. Technol. 117 (4) (1995) 483–493. doi:10.1115/1.2804743.

[48] E. Sanchez-Palencia, A. Zaoui, Homogenization Techniques for Composite Media, Springer Berlin Heidelberg, 1987. doi:10.1007/3-540-17616-0.

[49] Z.-P. Wang, L. H. Poh, Y. Zhu, J. Dirrenberger, S. Forest, Systematic design of tetra-petals auxetic structures with stiffness constraint, Mater. Des. 170 (2019) 107669. doi:10.1016/j.matdes.2019.107669.

[50] P.-O. Persson, G. Strang, A simple mesh generator in MATLAB, SIAM Review 46 (2) (2004) 329–345. doi:10.1137/s0036144503429121.

[51] H. W. Schreier, J.-J. Orteu, M. A. Sutton, Image Correlation for Shape, Motion and Deformation Measurements, Springer US, 2009. doi:10.1007/978-0-387-78747-3.

[52] M. A. Sutton, W. J. Wolters, W. H. Peters, W. F. Ranson, S. R. McNeill, Determination of displacements using an improved digital correlation method, Image Vis. Comput. 1 (3) (1983) 133–139. doi:10.1016/0262-8856(83)90064-1.

[53] Y. Sun, J. H. L. Pang, C. K. Wong, F. Su, Finite element formulation for a digital image correlation method, Appl. Opt. 44 (34) (2005) 7357. doi:10.1364/ao.44.007357.

[54] G. Besnard, F. Hild, S. Roux, "finite-element" displacement fields analysis from digital images: Application to portevin–le châtelier bands, Exp. Mech. 46 (6) (2006) 789–803. doi:10.1007/s11340-006-9824-8.

[55] F. Hild, S. Roux, Comparison of local and global approaches to digital image correlation, Exp. Mech. 52 (9) (2012) 1503–1519. doi:10.1007/s11340-012-9603-7.

[56] J. Rthor, A. Leygue, M. Coret, L. Stainier, E. Verron, Computational measurements of stress fields from digital images, Int. J. Numer. Methods Eng. 113 (12) (2017) 1810–1826. doi:10.1002/nme.5721.

[57] M. Mooney, A theory of large elastic deformation, J. Appl. Phys. 11 (9) (1940) 582–592. doi:10.1063/1.1712836.

[58] R. S. Rivlin, Large elastic deformations of isotropic materials. IV. further developments of the general theory, Philos. Trans. Royal Soc. A 241 (835) (1948) 379–397. doi:10.1098/rsta.1948.0024.

[59] E. A. Cerda, K. Ravi-Chandar, L. Mahadevan, Wrinkling of an elastic sheet under tension, Nature 419 (6907) (2002) 579–580. doi:10.1038/419579b.

[60] H. Wan, H. Ohtaki, S. Kotosaka, G. Hu, A study of negative poisson's ratios in auxetic honeycombs based on a large deflection model, Eur. J. Mech. A Solids 23 (1) (2004) 95–106. doi:10.1016/j.euromechsol.2003.10.006.

[61] U. Montanari, A method for obtaining skeletons using a quasi-euclidean distance, J. ACM 15 (4) (1968) 600–624. doi:10.1145/321479.321486.

[62] R. Kimmel, D. Shaked, N. Kiryati, A. M. Bruckstein, Skeletonization via distance maps and level sets, Comput. Vis. Image Underst. 62 (3) (1995) 382–391. doi:10.1006/cviu.1995.1062.

[63] M. Bornert, F. Brmand, P. Doumalin, J.-C. Dupré, M. Fazzini, M. Grédiac, F. Hild, S. Mistou, J. Molimard, J.-J. Orteu, L. Robert, Y. Surrel, P. Vacher, B. Wattrisse, Assessment of digital image correlation measurement errors: Methodology and results, Exp. Mech. 49 (3) (2008) 353–370. doi:10.1007/s11340-008-9204-7.

[64] Y. Q. Wang, M. A. Sutton, H. A. Bruck, H. W. Schreier, Quantitative error assessment in pattern matching: Effects of intensity pattern noise, interpolation, strain and image contrast on motion measurements, Strain 45 (2) (2009) 160–178. doi:10.1111/j.1475-1305.2008.00592.x.

[65] H. W. Schreier, J. R. Braasch, M. A. Sutton, Systematic errors in digital image correlation caused by intensity interpolation, Opt. Eng. 39 (11) (2000) 2915. doi:10.1117/1.1314593.

[66] B. Ling, K. Wei, Z. Wang, X. Yang, Z. Qu, D. Fang, Experimentally program large magnitude of poisson's ratio in additively manufactured mechanical metamaterials, Int. J. Mech. Sci. 173 (2020) 105466. doi:10.1016/j.ijmecsci.2020.105466.

[67] L. Luu, Z. Wang, M. Vo, T. Hoang, J. Ma, Accuracy enhancement of digital image correlation with b-spline interpolation, Opt. Lett. 36 (16) (2011) 3070. doi:10.1364/ol.36.003070.

[68] J.-C. Passieux, R. Bouclier, Classic and inverse compositional gauss-newton in global DIC, Int. J. Numer. Methods Eng. 119 (6) (2019) 453–468. doi:10.1002/nme.6057.

[69] L. Allais, M. Bornert, T. Bretheau, D. Caldemaison, Experimental characterization of the local strain field in a heterogeneous elastoplastic material, Acta Metall. Mater. 42 (11) (1994) 3865–3880. doi:10.1016/0956-7151(94)90452-9.

Appendix A. Small strain elasticity

Orthotropic symmetry with 2-d linear elasticity. Let us denote by Y the square domain of the unit cell depicted in Figure 1(b). From a mechanical point of view, the equivalent homogeneous material displays an effective orthotropic behaviour. The linear elastic constitutive equation averaged over the unit cell relating the mean stress and strain tensors, denoted as $\boldsymbol{\sigma}^H$ and $\boldsymbol{\varepsilon}^H$ respectively, has the following expression for the two dimensional problems under consideration:

$$\begin{aligned} &\boldsymbol{\sigma}^H = \mathbb{C}^H \boldsymbol{\varepsilon}^H \\ \text{where:}\quad &\boldsymbol{\sigma}^H = \langle \boldsymbol{\sigma} \rangle_Y , \qquad \boldsymbol{\varepsilon}^H = \langle \boldsymbol{\varepsilon} \rangle_Y . \\ &\mathbb{C}^H \text{ is the homogenised stiffness tensor} \end{aligned} \tag{A.1}$$

In two-dimensional elasticity, the components of $\mathbb{C}^H$ in matrix notation and in Cartesian coordinates read:

$$\begin{pmatrix} \sigma^H_{11} \\ \sigma^H_{22} \\ \sigma^H_{12} \end{pmatrix} = \begin{pmatrix} C^H_{1111} & C^H_{1122} & 0 \\ C^H_{1122} & C^H_{2222} & 0 \\ 0 & 0 & C^H_{1212} \end{pmatrix} \begin{pmatrix} \varepsilon^H_{11} \\ \varepsilon^H_{22} \\ 2\varepsilon^H_{12} \end{pmatrix} \tag{A.2}$$

Alternatively, one could express the effective strain as a function of the effective stress with the following effective material tensor:

$$\begin{pmatrix} \varepsilon^H_{11} \\ \varepsilon^H_{22} \\ 2\varepsilon^H_{12} \end{pmatrix} = \begin{pmatrix} 1/E_1 & -\nu_{12}/E_2 & 0 \\ -\nu_{21}/E_1 & 1/E_2 & 0 \\ 0 & 0 & 1/G \end{pmatrix} \begin{pmatrix} \sigma^H_{11} \\ \sigma^H_{22} \\ \sigma^H_{12} \end{pmatrix} \tag{A.3}$$

where E_i denote the homogenized Young moduli, ν_{ij} denote the Poisson's ratios and G denotes the homogenized shear modulus. Let us further remark, that by symmetry of the elastic compliance matrix, the following ratios have to be equal:

$$\frac{\nu_{12}}{E_2} = \frac{\nu_{21}}{E_1} \tag{A.4}$$

The elastic moduli, C^H_{ijkl}, can equally be expressed in terms of the compliance moduli, *i.e.* Young moduli and Poisson's ratios: $C^H_{1111} = (1 - \nu_{12}\nu_{21})^{-1} E_1$, $C^H_{2222} = (1 - \nu_{12}\nu_{21})^{-1} E_2$, $C^H_{1122} = \nu_{21}(1 - \nu_{12}\nu_{21})^{-1} E_1$, $C^H_{2211} = \nu_{12}(1 - \nu_{12}\nu_{21})^{-1} E_2$ with $C^H_{1122} = C^H_{2211}$ as can be easily obtained from the inversion of the corresponding matrices. A simple calculation immediately yields:

$$\nu_{12} = \frac{C^H_{1122}}{C^H_{2222}} \text{ and } \nu_{21} = \frac{C^H_{1122}}{C^H_{1111}}. \tag{A.5}$$

Moreover, the homogenized Poisson's ratio ν_{ij} are equally denoted *effective* Poisson's ratio to highlight their reference to the homogenized unit cell. For example ν_{12} characterizes the contraction of the structure in the direction of Oy axis when the cell stretched in the direction of Ox axis and in general $\nu_{12} \neq \nu_{21}$. Note that if the micro-architecture of the unit cell were to obey "cubic" symmetry, we would have $C^H_{1111} = C^H_{2222}$ and we would trivially obtain that $E_1 = E_2 = E^*$ and $\nu_{12} = \nu_{21} = \nu^*$.

$\mathbb{C}^H(\omega)$	$\mathbb{C}^{H,exp}(\omega)$
$\begin{pmatrix} 0.12 & -0.05 & 0 \\ -0.05 & 0.04 & 0 \\ 0 & 0 & 0.006 \end{pmatrix}$	$\begin{pmatrix} 0.1207 & -0.0487 & 0 \\ -0.0487 & 0.0318 & 0 \\ 0 & 0 & 0.0044 \end{pmatrix}$

Table A.1: Comparison between the effective $\mathbb{C}^H(\omega)$ (see also Table 1 of [36]) and measured elasticity tensor $\mathbb{C}^{H,exp}(\omega)$ displayed in the left and right column respectively. The measured elasticity tensor $\mathbb{C}^{H,exp}(\omega)$ was determined by combining DIC measurements and FEM computations.

Experimental identification of the elastic coefficients. Hereafter we provide the complete experimental measurement of the effective elastic stiffness tensor. Let us recall that the effective constitutive law (A.1) or alternatively (A.2) is a linear relation between the components of the effective stress and strain, from which the elastic moduli could be identified by a least square fitting. The main difficulty is that only the effective strain, $\boldsymbol{\varepsilon^H}$, can be directly measured from the experiment, see for instance Figure 7. However, as suggested in [56], the effective stress $\boldsymbol{\sigma^H}$ can be numerically computed from the experimental applied forces if the geometry and the constitutive behaviour of the base material are validated. As a consequence, $\mathbb{C}^H$, the effective elastic tensor of the design phase is obtained as a linear fit from $\boldsymbol{\varepsilon^H}$ and $\boldsymbol{\sigma^H}$. The computation could be performed on several unit cells of the specimen, yet here we will merely report the behaviour of the central unit cell. In order to compare the values of the elasticity tensor $\mathbb{C}^H$ computed in the design phase we have non-dimensionalised the resultant forces.

For the computations, the elastic moduli of the base material were fixed according to [36] for comparison purposes. Hence, the base material was defined with a Young's modulus $E_m = 0.91\,\text{MPa}$ and with a Poisson's ratio $\nu = 0.3$. Under the plane stress assumption, the components of the elastic tensor of the base material become $C^m_{1111} = C^{2222}_m = 1.0\,\text{MPa}$; $C^{1122}_m = 0.3\,\text{MPa}$; $C^{1212}_m = 0.35\,\text{MPa}$.

Experimentally, we remark that that T_1 is around four times stiffer than T_2 for an effective strain ranging from 0. to 0.1.

Appendix B. Digital Image Correlation

In the following paragraphs, a theoretical background and implementation details associated to the Digital Image Correlation methods implemented for the present work are presented.

Problem formulation. Given a *reference* image G and the *current* image g, DIC procedures aim at minimizing the following distance function:

$$\epsilon(\boldsymbol{x}) = \int_{\mathcal{D}} \Big[g(\boldsymbol{x}) - G(\boldsymbol{X}) \Big]^2 \, d\mathcal{D} \tag{B.1}$$

where $\boldsymbol{X}$ is the reference configuration, $\boldsymbol{x} = \boldsymbol{X} + \boldsymbol{u}$ is the current configuration, $\boldsymbol{u}$ is the displacement field and $\mathcal{D}$ is the *Region Of Interest* (ROI, see Figure B.9(a)).

Pixel interpolation. The images $G : \mathcal{D} \to \mathbb{R}$ and $g : \mathcal{D} \to \mathbb{R}$ are discrete-valued: their value is only known at integer pixel coordinates. However, both configurations $\boldsymbol{X}$ and $\boldsymbol{x}$ take *real values*, thus requiring the images to be probed at non-integer coordinates in order to evaluate the cost function (B.1). Various interpolation schemes can be implemented [65, 67], ranging from simple bilinear to bi-quintic B-spline approximations.

Discretisation. In order to solve the minimization problem associated to the cost function (B.1), the displacement field $\boldsymbol{u}$ is discretised as follows:

$$\boldsymbol{u}(\boldsymbol{X}) = \boldsymbol{N}(\boldsymbol{X}) \cdot \{\boldsymbol{u}\} \tag{B.2}$$

where $\boldsymbol{N} : \mathcal{D} \to \mathbb{R}^2$ denotes a set of *shape functions* and $\{\boldsymbol{u}\}$ is the finite set of parameters to be determined.

Local DIC. In the *local* approach, the image is divided in a number of K *small subdomains* $\Omega_k \subset \mathcal{D}$, $k = 1 \ldots, K$ (see Figure B.9(b)). In each sub-domain, elementary displacement fields are taken, associated to simple shape functions. In the present work, a *uniform* displacement $\boldsymbol{U}_k$ is assumed in each sub-domain Ω_k, corresponding to $\boldsymbol{N}(\boldsymbol{X}) = \boldsymbol{I}$, thus leading to the K following cost functions, for $k = 1, \ldots, K$:

$$\epsilon_\ell(\boldsymbol{U}_k) = \int_{\Omega_k} \Big[g(\boldsymbol{X} + \boldsymbol{U}_k) - G(\boldsymbol{X}) \Big]^2 \, d\Omega \tag{B.3}$$

that are to be minimized *independently*. In this formulation, the $2K$ parameters $\{\boldsymbol{u}\}_k = \boldsymbol{U}_k$ to be determined correspond to the *mean displacement* in each sub-domain Ω_k.

Global DIC. The *global* formulation is based on shape functions defined on the *entire* region of interest $\mathcal{D}$. In this work, piecewise-linear functions $\boldsymbol{N}(\boldsymbol{X})$ are taken as the shape functions of a finite element mesh $\mathcal{M}^{DIC}$ (see Fig. B.9.c) composed of N nodes connected by linear triangles, thus leading to the following cost function:

$$\epsilon_g(\{\boldsymbol{u}\}) = \int_{\mathcal{D}} \Big[g(\boldsymbol{X} + \boldsymbol{N}(\boldsymbol{X}) \cdot \{\boldsymbol{u}\}) - G(\boldsymbol{X}) \Big]^2 \, d\mathcal{D} \tag{B.4}$$

where the $2N$ parameters $\{\boldsymbol{u}\}$ to be determined correspond to the *nodal displacements*.

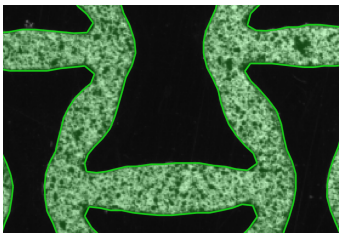

(a) Region Of Interest $\mathcal{D}$

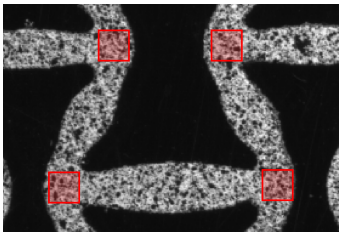

(b) Local subdomains Ω_k

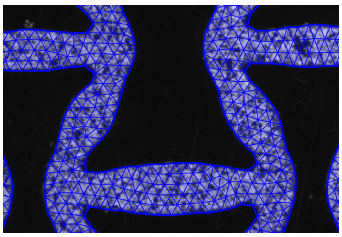

(c) Global mesh $\mathcal{M}^{DIC}$

Figure B.9: Geometries associated to digital image correlation.

Regularization. In contrast to the local formulation where the parameters $\boldsymbol{U}_k$ are determined independently, the parameters $\{\boldsymbol{u}\}$ are determined *simultaneously* in the global formulation. This enables to introduce an additional term in the global cost function ϵ_g (B.4) associated to a Tikhonov regularization of the strain field $\boldsymbol{\varepsilon}(\boldsymbol{X})$. Introducing the matrix $\boldsymbol{B}(\boldsymbol{X}) = \mathrm{sym}\,(\nabla_{\boldsymbol{X}} \boldsymbol{N}(\boldsymbol{X}))$ so that $\boldsymbol{\varepsilon}(\boldsymbol{X}) = \boldsymbol{B}(\boldsymbol{X}) \cdot \{\boldsymbol{u}\}$, the regularized cost functions is expressed as:

$$\epsilon_r(\{\boldsymbol{u}\}) = \epsilon_g(\{\boldsymbol{u}\}) + \beta \int_{\mathcal{D}} \Big\| \nabla_{\boldsymbol{X}} \boldsymbol{B}(\boldsymbol{X}) \cdot \{\boldsymbol{u}\} \Big\|^2 \, d\mathcal{D} \tag{B.5}$$

where the parameter β is fixed *a priori* and is a compromise between the regularized strain smoothness (higher values of β) and the image difference minimization (lower values of β). However, as linear elements are used in this work, the strains are *uniform* in each triangle, thus the strain gradient *vanishes*. To get around the problem, the strain *gap* between two attached triangles is used instead. Hence the regularization is formulated using the mesh *interior edges* (edges e with two connected triangles $t_{e,1}$ and $t_{e,2}$), leading to the following cost function:

$$\begin{aligned} \epsilon_r(\{\boldsymbol{u}\}) &= \epsilon_g(\{\boldsymbol{u}\}) + \beta \sum_e \Big\| \Delta \boldsymbol{B}_e \cdot \{\boldsymbol{u}\} \Big\|^2 \\ \text{with} \quad \Delta \boldsymbol{B}_e &= \frac{\boldsymbol{B}(\boldsymbol{C}_{e,1}) - \boldsymbol{B}(\boldsymbol{C}_{e,2})}{\Big\| \boldsymbol{C}_{e,1} - \boldsymbol{C}_{e,2} \Big\|} \end{aligned} \tag{B.6}$$

where $C_{e,n}$ denotes the centroid of the triangle $t_{e,n}$.

Gauss-Newton minimization algorithm. A Gauss-Newton algorithm is implemented to determine the parameters that minimize the cost functions (B.3), (B.4) or (B.5). Starting from an *initial guess* $\{\boldsymbol{u}^0\} = \boldsymbol{0}$, the parameter update is given by:

$$\{\boldsymbol{u}^{i+1}\} = \{\boldsymbol{u}^i\} - \boldsymbol{H}_i^{-1} \cdot \boldsymbol{j}_i \tag{B.7}$$

where $\boldsymbol{j}$ and $\boldsymbol{H}$ are, respectively, the *Jacobian* and the pseudo-*Hessian* associated to the cost functions ϵ. Noting that $\partial g(\boldsymbol{x})/\partial\{\boldsymbol{u}\} = \nabla_{\boldsymbol{x}} g(\boldsymbol{x}) \cdot \boldsymbol{N}(\boldsymbol{X})$, they are expressed as:

$$\boldsymbol{j}_i = \int_{\mathcal{D}} {}^{\top}\Big(\nabla_{\boldsymbol{x}^i} g(\boldsymbol{x}^i) \cdot \boldsymbol{N}(\boldsymbol{X})\Big) \cdot \Big[g(\boldsymbol{x}^i) - G(\boldsymbol{X})\Big]\, d\mathcal{D} \tag{B.8}$$

$$\boldsymbol{H}_i = \int_{\mathcal{D}} {}^{\top}\Big(\nabla_{\boldsymbol{x}^i} g(\boldsymbol{x}^i) \cdot \boldsymbol{N}(\boldsymbol{X})\Big) \cdot \Big(\nabla_{\boldsymbol{x}^i} g(\boldsymbol{x}^i) \cdot \boldsymbol{N}(\boldsymbol{X})\Big)\, d\mathcal{D} \tag{B.9}$$

with $\boldsymbol{x}^i = \boldsymbol{X} + \boldsymbol{N}(\boldsymbol{X}) \cdot \{\boldsymbol{u}^i\}$ and where the domain $\mathcal{D}$ and the shape functions $\boldsymbol{N}(\boldsymbol{X})$ depend on the chosen formulation. The global regularization terms introduced in (B.6) requires the modification of the preceding expressions as follows:

$$\boldsymbol{j}_i^r = \boldsymbol{j}_i + \beta \sum_e {}^{\top}\Delta\boldsymbol{B}_e \cdot \Delta\boldsymbol{B}_e \cdot \{\boldsymbol{u}^i\} \tag{B.10}$$

$$\boldsymbol{H}_i^r = \boldsymbol{H}_i + \beta \sum_e {}^{\top}\Delta\boldsymbol{B}_e \cdot \Delta\boldsymbol{B}_e \tag{B.11}$$

This updating procedure is repeated until convergence. The norm of the parameter update has been chosen here as the convergence criterion, as follows:

$$\| \{\boldsymbol{u}^{i+1}\} - \{\boldsymbol{u}^i\} \| < \delta \tag{B.12}$$

where δ is taken as a small fraction of a pixel, depending on the quality of the images and the desired accuracy.

Image gradient estimation. The image gradient $\nabla_{\boldsymbol{x}} g(\boldsymbol{x})$ is required in the Jacobian (B.8) and the Hessian (B.9). This is performed here using a second order finite-differences scheme. However, the drawback of the update (B.7) is that it uses the gradient of the *current* image g with respect to the *current* configuration $\boldsymbol{x}^i$. As a consequence, it has to be evaluated at each iteration, thus leading to a high computational burden (differentiation followed by interpolation). In order to get around the problem, a *modified* Gauss-Newton formulation can be formulated using the fact that, *sufficiently close* to the solution, $g(\boldsymbol{x}^i) \approx G(\boldsymbol{X})$ so that:

$$\nabla_{\boldsymbol{x}^i} g(\boldsymbol{x}^i) \approx \nabla_{\boldsymbol{X}} G(\boldsymbol{X}) \tag{B.13}$$

can be used to approximate the gradient of g with those of G in (B.8) and (B.9). The latter only needs to be computed once, at the beginning of the DIC procedure, thus drastically reducing the computationnal cost of the algorithm. However, the approximation in (B.13) only holds for *small* rotational motions: when large rotations occur, this *modified* formulation does not converge [68] and the gradient of g has to be used instead.

Appendix C. Macroscopic strain computation

When the measurement the full strain field cannot be achieved using DIC, it is still possible to compute the mean strain over a domain, provided that its boundaries can be tracked. This is used in the present work to compute the mean macroscopic strain from the unit cell corner nodes only, as the strains in the unit cell voids cannot be estimated (refer to Figure 7). Following the procedure proposed by Bornert [69], we start by expressing the mean transformation gradient $\bar{\boldsymbol{F}}$ over a domain Ω as follows:

$$\bar{\boldsymbol{F}} = \langle \boldsymbol{F}(\boldsymbol{x}) \rangle_\Omega = \frac{1}{|\Omega|} \int_\Omega \left(\boldsymbol{I} + \frac{\partial \boldsymbol{u}}{\partial \boldsymbol{x}}\right) d\Omega \tag{C.1}$$

which can be transformed to a *boundary* integral using Green's theorem:

$$\bar{\boldsymbol{F}} = \boldsymbol{I} + \frac{1}{|\Omega|} \int_{\partial\Omega} \boldsymbol{u} \otimes \boldsymbol{n}\, d\ell \tag{C.2}$$

where $\otimes$ denotes the outer product and $\boldsymbol{n}$ is the outgoing normal to the contour $\partial\Omega$. Considering a domain Ω corresponding to a quadrilateral unit cell defined by its four corner points, this integral can be evaluated to retrieve the macroscopic transformation gradient. Finally, one can deduce the corresponding macroscopic Green-Lagrange strains $\bar{\boldsymbol{E}}$ as follows:

$$\bar{\boldsymbol{E}} = \frac{1}{2}\Big[{}^{\top}\bar{\boldsymbol{F}} \cdot \bar{\boldsymbol{F}} - \boldsymbol{I}\Big] \tag{C.3}$$